Coherent gradient sensing: a Fourier optics analysis and applications to fracture

Hareesh V. Tippur

A Fourier optics analysis for a recently developed lateral shearing interferometry—coherent gradient sensing—is presented. The governing equations for the method are explicitly derived. The method of coherent gradient sensing is particularly suitable for investigating the mechanics of fracture of transparent and opaque solids. Several examples demonstrating the applicability of the method to quasistatic and dynamic crack-growth problems is presented.

1. Introduction

In recent years several lateral shearing interferometers have been proposed.[1–13] The simplicity of implementation and the relative insensitivity to vibrations make them suitable for several engineering applications. Optical component testing,[2,3,11–13] range sensing,[6] nondestructive evaluation,[1] experimental stress, and strain analysis[4,5,7–10] are a few examples that indicate the wide variety of the engineering and scientific applications of shearing interferometry. These techniques essentially provide information pertaining to the derivatives of the object wave-front phase profile. The wave-front shearing is typically accomplished by using prisms, gratings, glass plates, or digital-image processing. Apart from the type of the shearing device used, shearing interferometers are also classified into single-exposure interferometers in which the resulting fringe patterns are observed in real time, and double-exposure interferometers wherein a subsequent spatial filtering, either optical or digital, is performed to recover the information pertaining to the object wave front.

Recently a real-time lateral grating shearing interferometry, coherent gradient sensing (CGS), was developed for investigating the fracture of engineering materials. CGS has been successfully applied to quasistatic and dynamic crack-growth studies of both transparent and opaque solids by the author and his associates.[14–17] One of the unique advantages of the method is that because it is a real-time technique, it can be easily applied to transient crack-growth studies when used in conjunction with a high-speed camera. The method has been successfully implemented with high-speed photography (framing rates of up to 150,000 frames/s) to freeze deformation fields near rapidly propagating cracks (crack velocities 300–1000 m/s). CGS provides an experimental alternative to techniques such as photoelasticity and caustics that are traditionally used for investigating the dynamic fracture of materials. As a full-field optical technique, CGS has definite advantages over the method of caustics. At the same time, it can still be used with optically isotropic materials, whereas photoelasticity requires birefringent models. In this paper a detailed Fourier optics analysis for the method of CGS is presented. The analysis is relatively comprehensive when compared with the method proposed earlier[14,15] in deriving the governing equations for the technique. Several examples to demonstrate the experimental feasibility of the method to the study of fracture mechanics of solids is also presented.

2. Experimental Method

A. Optical Setup

The schematic of the optical setup used for transmission CGS is shown in Fig. 1. A transparent, optically isotropic specimen is illuminated by a collimated bundle of laser light. The transmitted object wave is then incident on a pair of identical high-density, chromium-on-glass master gratings, G_1 and G_2, separated by a distance Δ. The light-field distribution on the G_2 plane is spatially filtered by the filtering lens L, and its frequency content is displayed on its back focal

Hareesh V. Tippur is with the Department of Mechanical Engineering, Auburn University, Auburn, Alabama 36849-5341.

Received 01/09/92.
0003-6935/92/224428-12$05.00/0.

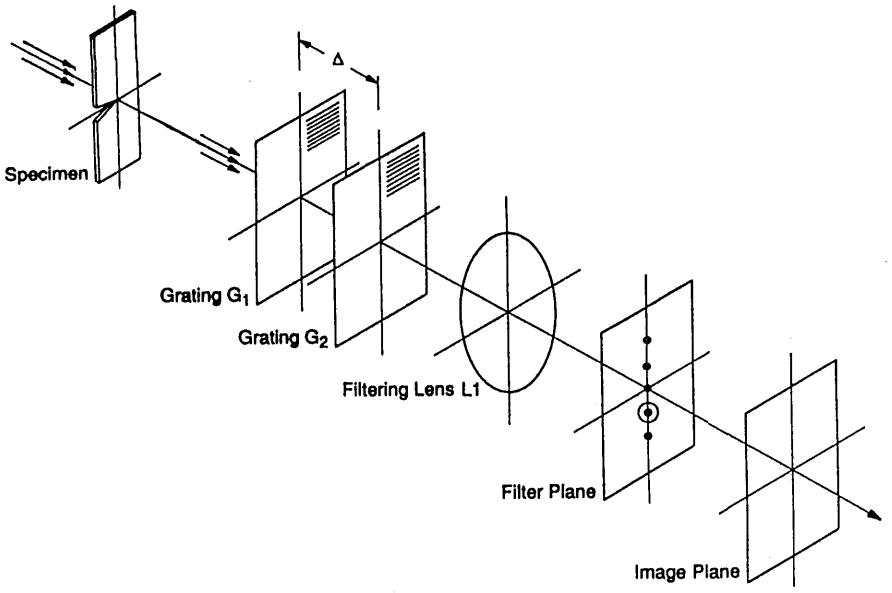

Fig. 1. Schematic for the experimental setup for transmission CGS.

plane. By locating a filtering aperture around either of the ±1 diffraction orders, we obtain information about stress gradients on the image plane of the lens L.

Figure 2 shows the modification of the above setup for measuring surface deflections of opaque solids when studied in the reflection mode. In this case, the specularly reflecting object surface is illuminated by a collimated beam of laser light with a beam splitter. As in the previous case, the reflected beam gets processed through the optical arrangement that is identical to the one shown in Fig. 1.

Figure 3 explains the working principle of the method of CGS. Let the line gratings have a square-wave transmittance. For the sake of simplicity, only zeroth-, first-, and negative first-order wave fronts are shown. Let the gratings G_1 and G_2 have their rulings parallel to, say, the x_0 axis. A plane wave transmitted through or reflected from an undeformed specimen and propagating along the optical axis is diffracted into three plane-wave fronts, E_0, E_1, and E_{-1}, by the first grating G_1. The magnitude of the angle between the propagation directions of E_0 and $E_{\pm 1}$ is given by the diffraction equation $\theta = \sin^{-1}(\lambda/p)$, where λ is the wavelength and p is the grating pitch. Upon incidence on the second grating G_2, the wave fronts are further diffracted into $E_{(0,0)}$, $E_{(0,1)}$, $E_{(1,-1)}$ $E_{(1,0)}$, $E_{(1,1)}$, and so on. These wave fronts,

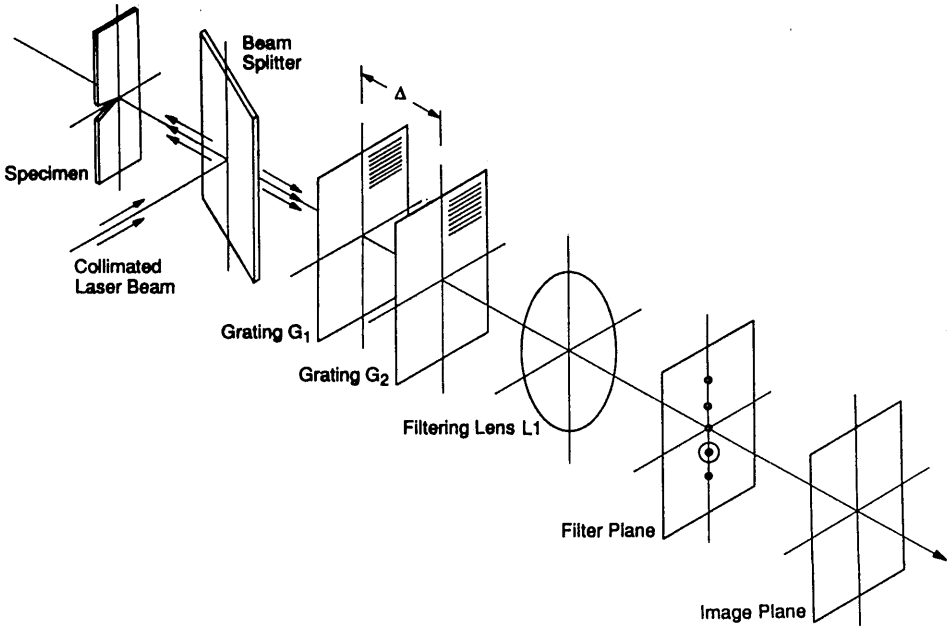

Fig. 2. Schematic for the experimental setup for reflection CGS.

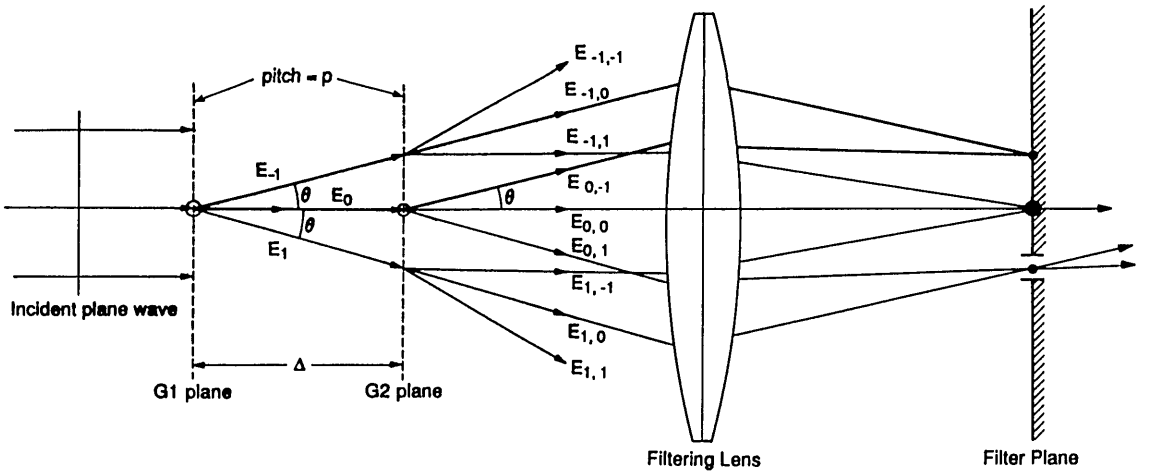

Fig. 3. Schematic describing the working principle of CGS.

which are propagating in distinctly different directions, are then brought to focus at spatially separated diffraction spots on the back focal plane of the filtering lens.

Now consider a plane wave normally incident on a deformed specimen surface. The resulting transmitted or reflected wave front will be distorted either because of changes of the refractive index or because of surface deformations. This object wave front incident on G_1 now carries information regarding the specimen deformation and consists of light rays traveling with small perturbations to their initial direction parallel to the optical axis. Thus, each of the diffraction spots on the focal plane of L will be locally surrounded by a halo of light because of the deflected light rays. The extent of the spread of the halo depends on the magnitude of the deformations. By using a filtering aperture at the focal plane of the lens, we image information existing around one of the spots on the image plane.

In subsection 2B, we present a Fourier analysis to demonstrate that the information contained in the interference patterns on the image plane corresponds to gradients of in-plane stress or to gradients of out-of-plane displacements.

B. Fourier Analysis

Figure 4 shows a two-dimensional schematic for CGS. The distance between the different planes of interest

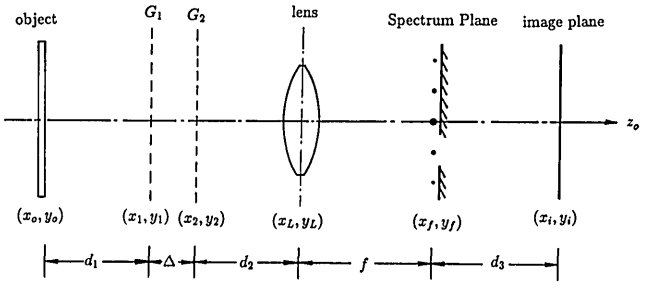

Fig. 4. Schematic describing the nomenclature used in the Fourier analysis.

along the optical axis is d_1, Δ, d_2, f, and d_3. Here f is the focal length of lens L, and the object $(d_1 + \Delta + d_2)$ and image $(f + d_3)$ distances satisfy the lens equation. The Cartesian coordinates (x_q, y_q) represent the in-plane coordinates of the object plane $(q = o)$, the grating planes $(q = 1$ and $q = 2)$, the lens plane $(q = \mathrm{L})$, the focal plane $(q = f)$, and the image plane $(q = i)$. Let $h_o(x_o, y_o)$ represent the complex amplitude distribution corresponding to the object plane. The amplitude distribution of light in front of the grating G_1 is $h_1(x_1, y_1)$. Using the Fresnel approximation for the wave propagation from the object plane to the front of the grating plane G_1, we find that

$$h_1(x_1,y_1) = h_o(x_1,y_1) \otimes g_{d_1}(x_1,y_1)$$
$$= h_o(x_1,y_1) \otimes \frac{1}{i\lambda d_1} \exp\left[ik\left(d_1 + \frac{x_1^2 + y_1^2}{2d_1}\right)\right], \quad (1)$$

where g_{d_1} is the point-source transfer function and $\otimes$ represents the convolution operation. Here k $(= 2\pi/\lambda)$ is the wave number and $i = \sqrt{-1}$. Let the grating G_1 have a relatively large aperture when compared with the size of the beam. For a square-wave grating, the transmittance function can then be approximated by $\Sigma A_m \exp(ikmy_1\theta)$, where $m = -\infty, \ldots, -3, -1, 0, 1, 3, \ldots, \infty$, A_m are constants and $\theta \approx (\lambda/p)$ for a small θ. Then the complex amplitude distribution immediately behind the grating G_1 is

$$h_1'(x_1, y_1) = \left\{h_o(x_1, y_1) \otimes \frac{1}{i\lambda d_1} \exp\left[ik\left(d_1 + \frac{x_1^2 + y_1^2}{2d_1}\right)\right]\right\}$$
$$\times \sum A_m \exp(ikmy_1\theta). \quad (2)$$

The diffracted wave front h_1' propagates to the second grating plane G_2, and the amplitude distribution immediately in front of G_2 is

$$h_2(x_2,y_2) = h_1'(x_2,y_2) \otimes \frac{1}{i\lambda\Delta} \exp\left[ik\left(\Delta + \frac{x_2^2 + y_2^2}{2\Delta}\right)\right]. \quad (3)$$

If $\sum A_n \exp(ikny_2\theta)$, $n = -\infty, \ldots, -3, -1, 0, 1, 3, \ldots, \infty$ represents the transmittance of the second grating G_2, the diffracted wave immediately behind the grating plane G_2 is

$$h_2'(x_2, y_2) = h_2(x_2, y_2) \times \sum A_n \exp(ikny_2\theta). \quad (4)$$

Substituting for $h_2(x_2, y_2)$ in Eq. (4) from Eqs. (1)–(3), we find

$$h_2'(x_2,y_2) = \left[\left(\left\{h_o(x_2,y_2) \otimes \frac{1}{i\lambda d_1} \exp\left[ik\left(d_1 + \frac{x_2^2 + y_2^2}{2d_1}\right)\right]\right\} \times \sum A_m \exp(ikmy_2\theta)\right) \otimes \frac{1}{i\lambda\Delta} \exp\left[ik\left(\Delta + \frac{x_2^2 + y_2^2}{2\Delta}\right)\right]\right] \times \sum A_n \exp(ikny_2\theta). \quad (5)$$

Now, using the Fourier transforming property of thin lenses, we can obtain frequency spectrum of the above complex amplitude distribution on the focal plane of the lens L as follows[18,19]:

$$h_f(x_f,y_f) = \frac{1}{i\lambda f} \exp[ik(f + d_2)] \exp\left[ik\left(\frac{x_f^2 + y_f^2}{2f}\right)\left(1 - \frac{d_2}{f}\right)\right] \times H_2'(w_x, w_y). \quad (6)$$

In Eq. (6) H_2' represents the Fourier transform $\mathcal{F}[h_2'(x_2, y_2)]$, and ($w_x = x_f/\lambda f$, $w_y = y_f/\lambda f$) denotes the coordinates of the spectral plane. Hence,

$$\mathcal{F}[h_2'(x_2, y_2)] = \mathcal{F}\left[\left(\left\{h_o(x_2, y_2) \otimes \frac{1}{i\lambda d_1} \times \exp\left[ik\left(d_1 + \frac{x_2^2 + y_2^2}{2d_1}\right)\right]\right\} \times \sum A_m \exp(ikmy_2\theta)\right) \otimes \frac{1}{i\lambda\Delta} \exp\left[ik\left(\Delta + \frac{x_2^2 + y_2^2}{2\Delta}\right)\right]\right] \otimes \sum B_n \delta\left(w_x, w_y - \frac{n\theta}{\lambda}\right), \quad (7)$$

where B_n's are the new constants after the Fourier transform operation and δ is the Dirac function. By successively carrying out the Fourier transform of the function in the square brackets (see Ref. 20), we can write Eq. (7) as

$$\mathcal{F}[h_2'(x_2, y_2)] = \left(\left\{[H_o(w_x, w_y) \times \exp(ikd_1 - i\pi\lambda d_1 \times \{w_x^2 + w_y^2\})] \otimes \sum B_m \delta\left(w_x, w_y - \frac{m\theta}{\lambda}\right)\right\} \times \exp(ik\Delta - i\pi\lambda\Delta\{w_x^2 + w_y^2\})\right) \otimes \sum B_n \delta\left(w_x, w_y - \frac{n\theta}{\lambda}\right), \quad (8)$$

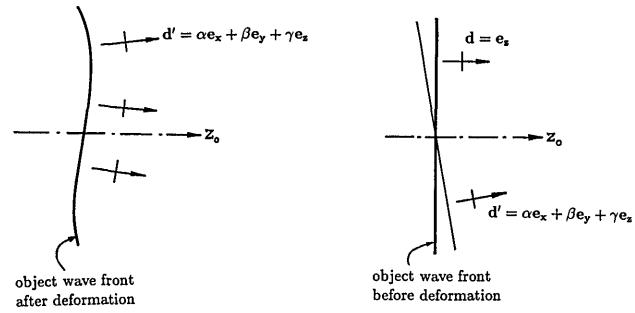

Fig. 5. Undeformed and deformed object wave fronts.

$$= \exp[ik(d_1 + \Delta)]\left[\left(\sum B_m H_o\left(w_x, w_y - \frac{m\theta}{\lambda}\right) \times \exp\left\{-i\pi\lambda d_1\left[w_x^2 + \left(w_y - \frac{m\theta}{\lambda}\right)^2\right]\right\}\right) \times \exp(-i\pi\lambda\Delta\{w_x^2 + w_y^2\})\right] \otimes \sum B_n \delta\left(w_x, w_y - \frac{n\theta}{\lambda}\right). \quad (9)$$

Further simplification of Eq. (9) is possible if certain features of the input function h_o are known *a priori*. One of the simplest forms of h_o corresponds to a plane wave originating from a specimen that is specularly reflective or transparent. Then the object wave front is (1) planar, and its propagation vector is parallel to the optical axis (z_o axis) when the specimen is undeformed, and (2) perturbed locally, say near a crack tip, when subjected to external loads as shown in Fig. 5. These perturbations are caused by nonuniform surface slopes in the case of reflective specimens, whereas they are caused by a combination of nonuniform specimen-thickness changes and refractive-index changes in the case of transparent specimens. In both cases the propagating object wave front can be viewed to be made of locally collimated bundles of rays with direction cosines α, β, and γ (Fig. 5).

To understand the formation of interference fringe further, consider, for simplicity and without losing generality, a plane wave whose complex amplitude distribution on (x_o, y_o, $z_o = 0$) is

$$h_o(x_o, y_o, z_o = 0) = C \exp[ik\mathbf{d}' \cdot (x_o\hat{e}_x + y_o\hat{e}_y)] = C \exp[ik(\alpha x_o + \beta y_o)], \quad (10)$$

where C is a constant, $\hat{e}_x$, $\hat{e}_y$, and $\hat{e}_z$ are unit vectors in the x_o, y_o, and z_o directions, respectively, and the propagation vector for the wave front $\mathbf{d}'$ is

$$\mathbf{d}' = \alpha\hat{e}_x + \beta\hat{e}_y + \gamma\hat{e}_z. \quad (11)$$

Hence,

$$H_o\left(w_x, w_y - \frac{m\theta}{\lambda}\right) = \delta\left(w_x - \frac{\alpha}{\lambda}, w_y - \frac{m\theta + \beta}{\lambda}\right). \quad (12)$$

Using the multiplicative property of a Dirac function, namely $\Phi(x)\delta(x - x_a) = \Phi(x_a)\delta(x - x_a)$, we can simplify Eq. (9) to

$$\mathcal{F}[h_2'(x_2, y_2)] = \exp[ik(d_1 + \Delta)] \times \left(\sum B_m \delta\left(w_x - \frac{\alpha}{\lambda}, w_y - \frac{m\theta + \beta}{\lambda}\right) \times \exp\left\{-i\pi\lambda d_1\left[\left(\frac{\alpha}{\lambda}\right)^2 + \left(\frac{\beta}{\lambda}\right)^2\right]\right\} \times \exp\left\{-i\pi\lambda\Delta\left[\left(\frac{\alpha}{\lambda}\right)^2 + \left(\frac{m\theta + \beta}{\lambda}\right)^2\right]\right\}\right) \otimes \sum B_n \delta\left(w_x, w_y - \frac{n\theta}{\lambda}\right). \quad (13)$$

When carried out, the above convolution results in a series of discrete delta functions as detailed in Appendix A. If $\alpha = 0$, $\beta = 0$, and $\gamma = 1$ (the undeformed object wave front), the spatial-frequency spectrum essentially consists of a linear array of equally spaced delta functions. Thus, for small values of α and β, the deformed object wave front can be viewed as a perturbation of an undeformed wave front (Appendix A). By locating a filtering aperture centered around, say, $\delta(w_x, w_y - \theta/\lambda)$ [but large enough to permit small perturbations β (or α) surrounding it], we allow complex wave fronts corresponding to the third and seventh terms in Eq. (33) to propagate to the image plane of the optical system (Fig. 4). Hence the filtered information just behind the frequency plane is

$$H_2''(w_x, w_y) = B_o B_1 \exp[ik(d_1 + \Delta)] \times \exp\left\{-i\pi\lambda d_1\left[\left(\frac{\alpha}{\lambda}\right)^2 + \left(\frac{\beta}{\lambda}\right)^2\right]\right\} \times \left(\exp\left\{-i\pi\lambda\Delta\left[\left(\frac{\alpha}{\lambda}\right)^2 + \left(\frac{\beta - \theta}{\lambda}\right)^2\right]\right\} + \exp\left\{-i\pi\lambda\Delta\left[\left(\frac{\alpha}{\lambda}\right)^2 + \left(\frac{\beta}{\lambda}\right)^2\right]\right\}\right) \times \delta\left(w_x - \frac{\alpha}{\lambda}, w_y - \frac{\beta - \theta}{\lambda}\right). \quad (14)$$

Also note that if the object wave were to have originated from a diffusely reflecting or transmitting specimen, such discrete spots would not be generally visible. Instead, they would be replaced by overlapped halos corresponding to each diffracted wave front without clear demarkation on the filtering plane necessary for successful real-time spatial filtering. The degree of overlap and the size of the halo are strong functions of the surface characteristics and the optical roughness of such a specimen.

Hence, using Eq. (6), we find that the amplitude distribution immediately behind the frequency plane after filtering is

$$\begin{aligned} h_f'(x_f, y_f) &= \frac{B_o B_1}{i\lambda f} \exp[ik(d_1 + \Delta + d_2 + f)] \times \exp\left\{i\pi\lambda f\left(1 - \frac{d_2}{f}\right)(w_x^2 + w_y^2)\right\} \times \exp\left\{-i\pi\lambda(d_1 + \Delta)\left[\left(\frac{\alpha}{\lambda}\right)^2 + \left(\frac{\beta}{\lambda}\right)^2\right]\right\} \times \left[1 + \exp\left\{-i\pi\Delta\theta\left(\frac{-2\beta + \theta}{\lambda}\right)\right\}\right] \times \delta\left(w_x - \frac{\alpha}{\lambda}, w_y - \frac{\beta - \theta}{\lambda}\right) \\ &= \frac{B_o B_1}{i\lambda f} \exp[ik(d_1 + \Delta + d_2 + f)] \times \exp\left\{i\pi\lambda f\left(1 - \frac{d_2}{f}\right)\left[\left(\frac{\alpha}{\lambda}\right)^2 + \left(\frac{\beta - \theta}{\lambda}\right)^2\right]\right\} \times \exp\left\{-i\pi\lambda(d_1 + \Delta)\left[\left(\frac{\alpha}{\lambda}\right)^2 + \left(\frac{\beta}{\lambda}\right)^2\right]\right\} \times \left[1 + \exp\left\{-i\pi\Delta\theta\left(\frac{-2\beta + \theta}{\lambda}\right)\right\}\right] \times \delta\left(w_x - \frac{\alpha}{\lambda}, w_y - \frac{\beta - \theta}{\lambda}\right). \end{aligned} \quad (15)$$

This filtered information propagates to the image plane on which the amplitude distribution can be expressed as[18]

$$\begin{aligned} h_i(x_i, y_i) &= \exp\left\{ik\frac{x_i^2 + y_i^2}{2d_3}\right\} \times \mathcal{F}\left[h_f'(x_f, y_f) \times \frac{1}{i\lambda d_3} \exp\left\{ik\left(d_3 + \frac{x_f^2 + y_f^2}{2d_3}\right)\right\}\right] \\ &= -\frac{B_o B_1}{\lambda^2 f d_3} \exp\left\{ik\frac{x_i^2 + y_i^2}{2d_3}\right\} \times \exp[ik(d_1 + \Delta + d_2 + f + d_3)] \times \exp\left\{i\pi\lambda f\left(1 - \frac{d_2 + d_3}{f}\right)\left[\left(\frac{\alpha}{\lambda}\right)^2 + \left(\frac{\beta - \theta}{\lambda}\right)^2\right]\right\} \times \exp\left\{-i\pi\lambda(d_1 + \Delta)\left[\left(\frac{\alpha}{\lambda}\right)^2 + \left(\frac{\beta}{\lambda}\right)^2\right]\right\} \times \left[1 + \exp\left\{-i\pi\Delta\theta\left(\frac{-2\beta + \theta}{\lambda}\right)\right\}\right] \times \mathcal{F}\left[\delta\left(w_x - \frac{\alpha}{\lambda}, w_y - \frac{\beta - \theta}{\lambda}\right)\right], \end{aligned} \quad (16)$$

$$= C' \exp[ik\Psi] \times \left[1 + \exp\left\{-i\pi\Delta\theta\left(\frac{-2\beta + \theta}{\lambda}\right)\right\}\right] \times \exp\{-ik(x_i\alpha + y_i\beta)\}, \quad (17)$$

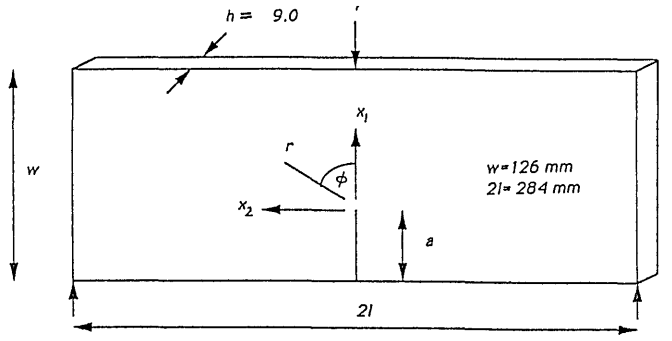

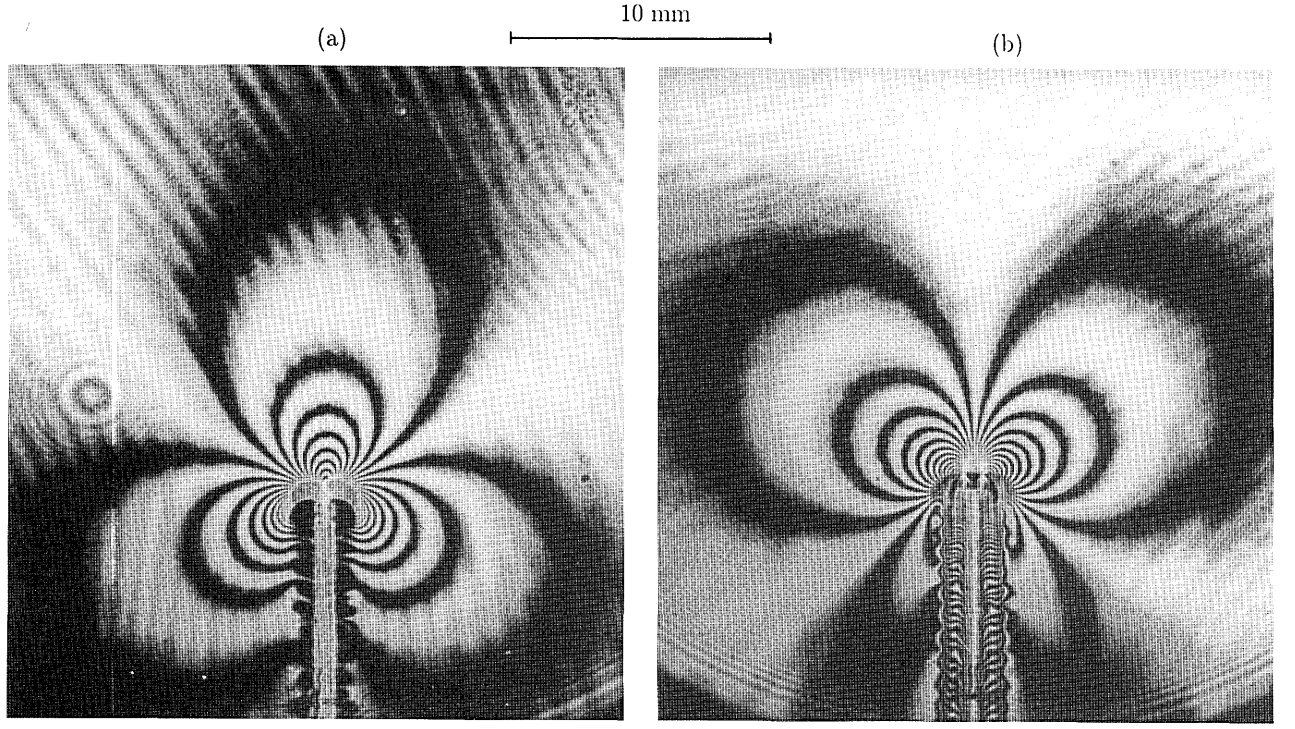

Fig. 6. Interference patterns obtained using transmission CGS: contours representing (a) $\partial(\sigma_{xx} + \sigma_{yy})/\partial x_o$ and (b) $\partial(\sigma_{xx} + \sigma_{yy})/\partial y_o$. Inset is specimen geometry.

where Ψ represents the combined phase of all the constant terms in the above equation and C' is a constant. Hence, the light-intensity distribution on the image plane is

$$I_i(x_i, y_i) = h_i h_i^* = 2C'\left[1 + \cos\left(\pi\Delta\theta\,\frac{2\beta - \theta}{\lambda}\right)\right], \quad (18)$$

where the asterisk denotes the complex conjugate. Equation (18) is maximum when

$$\pi\Delta\theta\,(2\beta - \theta/\lambda) = 2N'\pi, \qquad N' = 0, \pm 1, \pm 2, \ldots \quad (19)$$

or

$$\beta = \frac{N'p}{\Delta} + \frac{\theta}{2}. \quad (20)$$

In the above equation, note that θ is an experimental constant that depends on the density of the gratings and is independent of the quantities of interest, namely α and β. Hence, when β is a function of the in-plane coordinates of the object plane, the fringe under N' varies from point to point over a constant dc-like term, $\theta/2$. Thus, we could interpret the

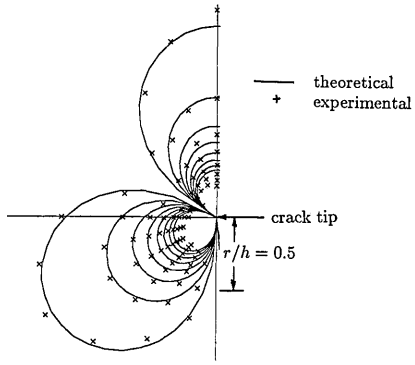

Fig. 7. Comparison between experimental data and analytical predictions for fringe patterns shown in Fig. 6(a).

fringe patterns simply as

$$\beta = \frac{Np}{\Delta}, \qquad N = 0, \pm 1, \pm 2, \ldots. \tag{21}$$

Now, by rotating the gratings G_1 and G_2 by 90°, we can shear the object wave front parallel to the x_o axis and α can be measured as follows:

$$\alpha = \frac{Mp}{\Delta}, \qquad M = 0, \pm 1, \pm 2, \ldots. \tag{22}$$

C. Relation Between Direction Cosines and Deformation

In this subsection, the direction cosines of the object wave front are related to the mechanical deformations of the specimen for both transmission and reflection cases.

For optically isotropic transparent solids, nonuniform thickness changes and refractive-index changes caused by mechanical loads introduce perturbations to the incident planar wave front. Under two-dimensional, linear elastic, plane-stress conditions, it can be shown that (see Ref. 15 for details) the propagation vector of the deformed object wave front is

$$\mathbf{d}' \approx \frac{\partial(\delta S)}{\partial x_o} e_x + \frac{\partial(\delta S)}{\partial y_o} e_y + e_z, \tag{23}$$

where the optical path change δS caused by combined refractive-index and thickness changes is

$$\delta S(x_o, y_o) \approx ch(\hat{\sigma}_{xx} + \hat{\sigma}_{yy}). \tag{24}$$

Here, c is the elasto-optical constant, h is the nominal thickness of the specimen and $\hat{\sigma}_{xx}$ and $\hat{\sigma}_{yy}$ represent the thickness averages of in-plane stress components. Comparing relation (23) and Eq. (11), we can deduce the governing equations for transmission CGS as follows:

$$ch \frac{\partial(\hat{\sigma}_{xx} + \hat{\sigma}_{yy})}{\partial x_o} \approx \frac{Mp}{\Delta}, \qquad M = 0, \pm 1, \pm 2, \ldots, \tag{25}$$

$$ch \frac{\partial(\hat{\sigma}_{xx} + \hat{\sigma}_{yy})}{\partial y_o} \approx \frac{Np}{\Delta}, \qquad N = 0, \pm 1, \pm 2, \ldots. \tag{26}$$

When the specimen is opaque, the surface is made initially flat and specularly reflective. After deformation, because of nonuniform surface-thickness changes, the incident wave front becomes nonplanar. Under linear elastic, plane-stress conditions, the propagation vector $\mathbf{d}'$ can be expressed in terms of specimen surface slopes as follows (see Ref. 15 for details):

$$\mathbf{d}' \approx 2 \frac{\partial w}{\partial x_o} e_x + 2 \frac{\partial w}{\partial y_o} e_y + e_z, \tag{27}$$

where w denotes the out-of-plane displacement of the specimen surface. By comparing Eq. (11) and relation (27), we can write the following governing equations for reflection CGS as follows:

$$\frac{\partial w}{\partial x_o} \approx \frac{Mp}{2\Delta}, \qquad M = 0, \pm 1, \pm 2, \ldots, \tag{28}$$

$$\frac{\partial w}{\partial y_o} \approx \frac{Np}{2\Delta}, \qquad N = 0, \pm 1, \pm 2, \ldots. \tag{29}$$

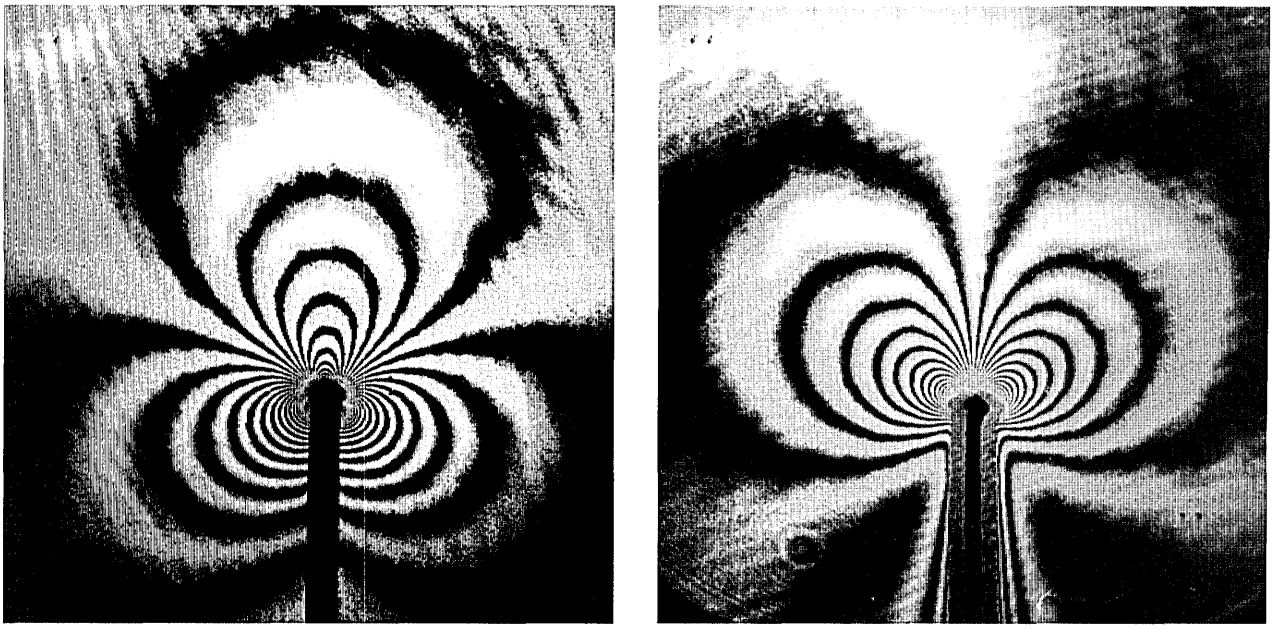

Fig. 8. Interference patterns obtained using reflection CGS: contours representing (a) $\partial w/\partial x_o$ and (b) $\partial w/\partial y_o$.

3. Applications to Fracture Mechanics

In this section we present examples demonstrating the applicability of CGS to the quasistatic and dynamic fracture of materials. The typical experimental parameters used are a grating separation distance Δ of 30 mm and a pitch p of the gratings equal to 0.025 mm. These parameters provide a sensitivity of measurement of 4.2×10^{-4} rad/fringe for transmission CGS and 2.1×10^{-4} rad/fringe for reflection CGS. Figure 6 shows optical interference patterns obtained using the transmission CGS technique from an edge-notched beam specimen undergoing symmetric three-point bending. The model is made from a polymethyl methacrylate (PMMA) sheet whose nominal thickness is 9 mm. The symmetric loading of the specimen results in opening-mode or mode-I deformations near the crack tip. The fringes represent contours of the crack-tip deformation fields, $ch\ \partial(\hat{\sigma}_{xx} + \hat{\sigma}_{yy})/\partial x_o$ and $ch\ \partial(\hat{\sigma}_{xx} + \hat{\sigma}_{yy})/\partial y_o$. For a two-dimensional, linear elastic, K-dominant, mode-I crack- tip field, the following relationship exists between the experimental measurements and the theoretical predictions[15,21]:

$$ch\frac{\partial(\hat{\sigma}_{xx} + \hat{\sigma}_{yy})}{\partial x_o} = ch\,\frac{K_I}{\sqrt{2\pi}}\,r^{-3/2}\cos(3\phi/2) + O(r^{-1/2}) = \frac{MP}{\Delta}, \tag{30}$$

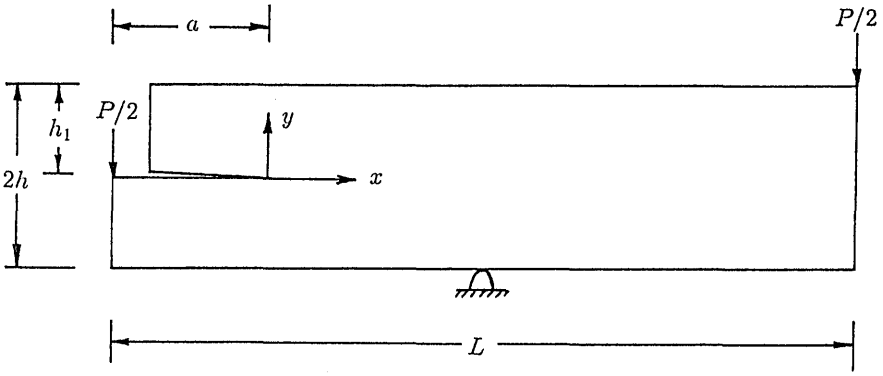

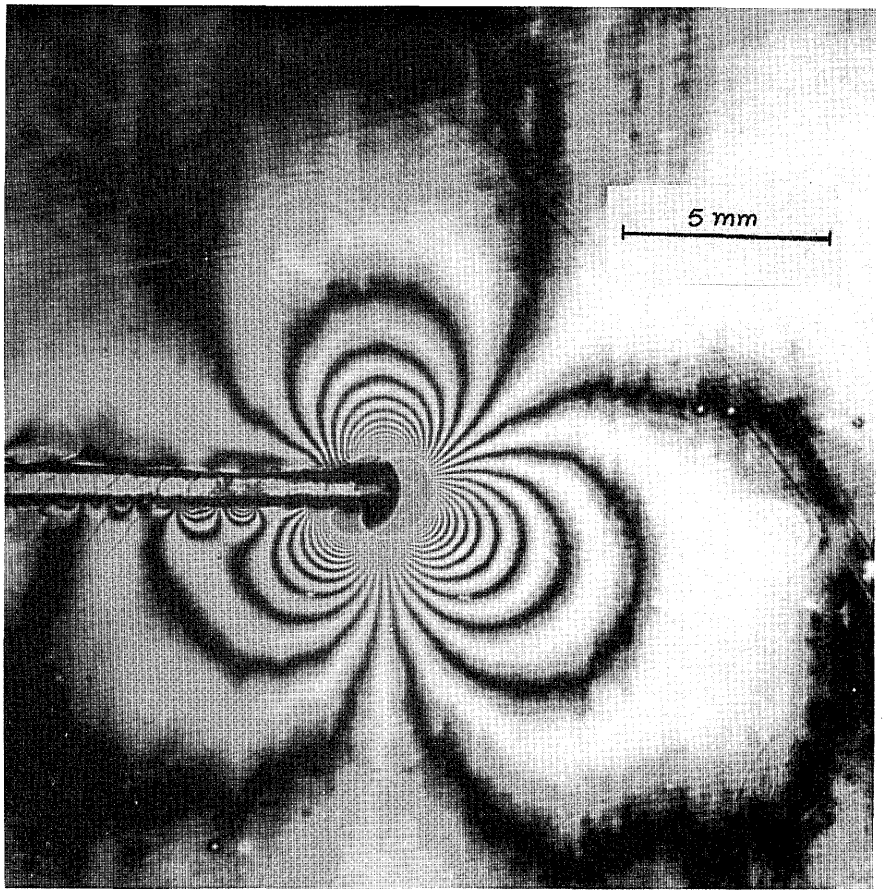

Fig. 9. Interference fringes obtained using transmission CGS with a modified fracture specimen; mixed-mode fringes representing contours of constant $\partial(\sigma_{xx} + \sigma_{yy})/\partial x_o$.

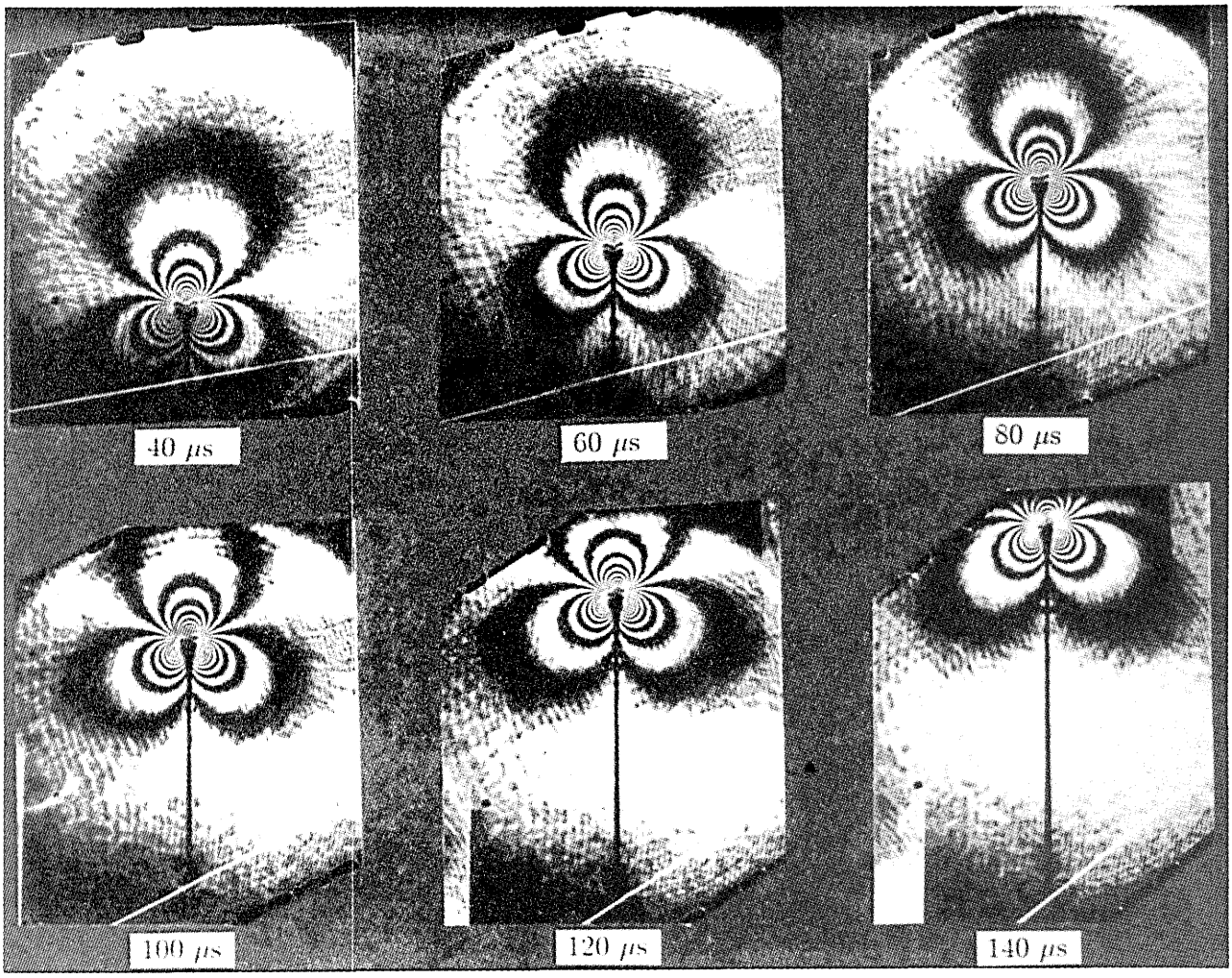

Fig. 10. Time sequence of $\partial(\sigma_{xx} + \sigma_{yy})/\partial x_o$, fringes near a dynamically growing crack in PMMA (transmission CGS).

$$ch\frac{\partial(\hat{\sigma}_{xx} + \hat{\sigma}_{yy})}{\partial y_o} = ch\frac{K_I}{\sqrt{2\pi}}r^{-3/2}\sin(3\phi/2) + O(r^{-1/2}) = \frac{Np}{\Delta}, \quad (31)$$

where K_I is the mode-I stress-intensity factor and (r, ϕ) denote the crack-tip polar coordinates. The fringe patterns are digitized to measure $[M \text{ (or } N), r, \phi]$ and extract K_I using least-squares data analysis. In Fig. 7, experimental data (crosses) are shown along with the theoretical prediction based on the boundary load measurement.[22] The agreement between the two is good in regions $0.5 \leq r/h \leq 1.25$. The disagreement in the region $0 \leq r/h \leq 0.5$, particularly ahead of the crack tip, is caused by the break down of the two-dimensional assumptions close to the crack tip where three-dimensional deformations[23] are dominant. The interference patterns from similar tests performed with a PMMA specimen using

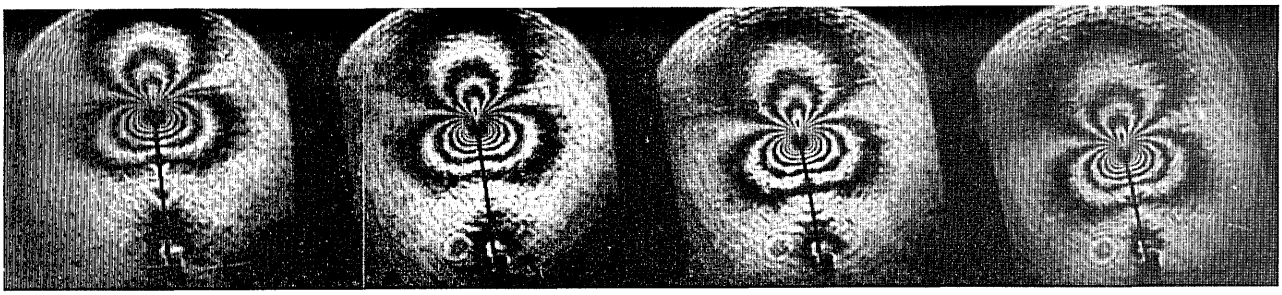

Fig. 11. Time sequence of $\partial w/\partial x_o$ near a dynamically growing crack in PMMA (reflection CGS); interframe time = 7 μs.

reflection CGS is shown in Fig. 8. Commercially available PMMA sheets have approximately 5–7% reflectance per surface. This feature is used in obtaining the crack-tip interference patterns representing contours of the deformation fields, $\partial w/\partial x_o$, $\partial w/\partial y_o$. The rear-surface reflections are simply cutoff by coating the back surface of the specimen with a spray of flat white paint.

The application of CGS can be easily extended to the study of the mixed-mode fracture of materials. The contours of the crack-tip field $ch\ \partial(\hat{\sigma}_{xx} + \hat{\sigma}_{yy})/\partial x_o$ when the crack is subjected to a combination of symmetric and antisymmetric loading or mixed-mode (mode-I plus mode-II) loading is shown in Fig. 9. A modified fracture specimen with a horizontal edge notch (see Fig. 9) is subjected to three-point bending. The crack tip undergoes a combination of opening and shear deformations, which is manifested in the rotation of the fringes about the crack tip as seen. When the crack-tip fields are under K-dominant, two-dimensional linear elastic conditions,[21] the fringe patterns can be analyzed using

$$ch\frac{\partial(\hat{\sigma}_{xx} + \hat{\sigma}_{yy})}{\partial x_o} = ch\frac{1}{\sqrt{2\pi}}r^{-3/2} \times [K_{\mathrm{I}}\cos(3\phi/2) - K_{\mathrm{II}}\sin(3\phi/2)] + O(r^{-1/2}) = \frac{Mp}{\Delta}, \tag{32}$$

where K_{II} is the mode-II stress-intensity factor.

As we mentioned in section 1, being a real-time experimental method, CGS can be readily applied to the study of the dynamic fracture of solids. In the examples presented here, CGS is used in conjunction with a continuous-access high-speed streak camera and a cavity-dumped argon–ion pulsed-laser light source. The typical repetition rate of the light pulse is 7–10μs (100,000–150,000 frames/s) with a pulse width of 50 ns used to freeze the unloading stress waves in materials caused by rapidly growing cracks. Dynamic crack growth is achieved by impact loading three-point bend specimens in a drop-weight tower with impact velocities in the range of 2–5 m/s. The stress-wave loading of a precut notch results in a dynamic crack initiation and a subsequent dynamic crack growth. The loading and the specimen configurations provide mode-I conditions for crack growth. In Fig. 10 a time sequence of a crack-tip fringe pattern corresponding to the propagation of a crack in PMMA obtained using transmission CGS is shown. The crack velocity is constant in the region of observation and is approximately 300 m/s. In Fig. 11 the time sequence of the fringe patterns obtained using reflection CGS from a reflective PMMA specimen is shown. Here the specimen is made reflective by depositing a thin layer of aluminum on the test surface by using the vacuum deposition process. Using dynamic, linear elastic, crack-tip field equations, similar to the quasistatic relations discussed earlier, we could extract dynamic stress-intensity factors from these transient deformation fields (see Ref. 16 for details).

4. Conclusions

A detailed Fourier optic analysis for a lateral shearing interferometric technique, coherent gradient sensing, is presented. The governing equations for the method in both transmission and reflection modes are explicitely derived. The propagation of the complex amplitudes through the various optical elements leading to the formation of interference fringes, which are related to the object wave-front perturbations, are analyzed. The analysis suggests that the object wave front should indeed originate from a specularly reflective or a transparent solid in order to obtain interference patterns in real time using conventional spatial filtering. Several examples to demonstrate the suitability of CGS to fracture mechanics of solids are presented. It is evident from the dynamic crack-growth examples that the real-time capability of CGS, when coupled with high-speed photography, provides an effective experimental tool for the study of crack propagation in general and dynamic fracture of solids in particular.

Appendix A

Equation (13) can be expanded through m, $n = 0, \pm 1, \pm 3, \pm 5 \ldots, \infty$. Here, for the sake of simplicity and brevity, expansion up to ± 1 is shown. The results remain unaffected even when expanded to higher values of m and n:

$$\begin{aligned}\mathcal{F}[h_2'(x_2, y_2)] = {} & \exp[ik(d_1 + \Delta)] \\ & \times \exp\left\{-i\pi\lambda d_1\left[\left(\frac{\alpha}{\lambda}\right)^2 + \left(\frac{\beta}{\lambda}\right)^2\right]\right\} \\ & \times \left(B_o \exp\left\{-i\pi\lambda\Delta\left[\left(\frac{\alpha}{\lambda}\right)^2 + \left(\frac{\beta}{\lambda}\right)^2\right]\right\}\right. \\ & \times \delta\left(w_x - \frac{\alpha}{\lambda}, w_y - \frac{\beta}{\lambda}\right) \\ & + B_1 \exp\left\{-i\pi\lambda\Delta\left[\left(\frac{\alpha}{\lambda}\right)^2 + \left(\frac{\beta + \theta}{\lambda}\right)^2\right]\right\} \\ & \times \delta\left(w_x - \frac{\alpha}{\lambda}, w_y - \frac{\beta + \theta}{\lambda}\right) \\ & + B_1 \exp\left\{-i\pi\lambda\Delta\left[\left(\frac{\alpha}{\lambda}\right)^2 + \left(\frac{\beta - \theta}{\lambda}\right)^2\right]\right\} \\ & \times \left.\delta\left(w_x - \frac{\alpha}{\lambda}, w_y - \frac{\beta - \theta}{\lambda}\right) + \cdots\right) \\ & \otimes \left[B_o\delta(w_x, w_y) + B_1\delta\left(w_x, w_y - \frac{\theta}{\lambda}\right)\right. \\ & \left. + B_1\delta\left(w_x, w_y + \frac{\theta}{\lambda}\right) + \cdots\right]\end{aligned}$$

$$
\begin{aligned}
&= \exp[ik(d_1 + \Delta)] \\
&\quad \times \exp\left\{-i\pi\lambda d_1\left[\left(\frac{\alpha}{\lambda}\right)^2 + \left(\frac{\beta}{\lambda}\right)^2\right]\right\} \\
&\quad \times \left(B_o^2 \exp\left\{-i\pi\lambda\Delta\left[\left(\frac{\alpha}{\lambda}\right)^2 + \left(\frac{\beta}{\lambda}\right)^2\right]\right\}\right. \\
&\quad \times \delta\left(w_x - \frac{\alpha}{\lambda}, w_y - \frac{\beta}{\lambda}\right) \\
&\quad + B_o B_1 \exp\left\{-i\pi\lambda\Delta\left[\left(\frac{\alpha}{\lambda}\right)^2 + \left(\frac{\beta + \theta}{\lambda}\right)^2\right]\right\} \\
&\quad \times \delta\left(w_x - \frac{\alpha}{\lambda}, w_y - \frac{\beta + \theta}{\lambda}\right) \\
&\quad + B_o B_1 \exp\left\{-i\pi\lambda\Delta\left[\left(\frac{\alpha}{\lambda}\right)^2 + \left(\frac{\beta - \theta}{\lambda}\right)^2\right]\right\} \\
&\quad \times \delta\left(w_x - \frac{\alpha}{\lambda}, w_y - \frac{\beta - \theta}{\lambda}\right) \\
&\quad + B_o B_1 \exp\left\{-i\pi\lambda\Delta\left[\left(\frac{\alpha}{\lambda}\right)^2 + \left(\frac{\beta}{\lambda}\right)^2\right]\right\} \\
&\quad \times \delta\left(w_x - \frac{\alpha}{\lambda}, w_y - \frac{\beta + \theta}{\lambda}\right) \\
&\quad + B_1^2 \exp\left\{-i\pi\lambda\Delta\left[\left(\frac{\alpha}{\lambda}\right)^2 + \left(\frac{\beta + \theta}{\lambda}\right)^2\right]\right\} \\
&\quad \times \delta\left(w_x - \frac{\alpha}{\lambda}, w_y - \frac{\beta + 2\theta}{\lambda}\right) \\
&\quad + B_1^2 \exp\left\{-i\pi\lambda\Delta\left[\left(\frac{\alpha}{\lambda}\right)^2 + \left(\frac{\beta - \theta}{\lambda}\right)^2\right]\right\} \\
&\quad \times \delta\left(w_x - \frac{\alpha}{\lambda}, w_y - \frac{\beta}{\lambda}\right) \\
&\quad + B_o B_1 \exp\left\{-i\pi\lambda\Delta\left[\left(\frac{\alpha}{\lambda}\right)^2 + \left(\frac{\beta}{\lambda}\right)^2\right]\right\} \\
&\quad \times \delta\left(w_x - \frac{\alpha}{\lambda}, w_y - \frac{\beta - \theta}{\lambda}\right) \\
&\quad + B_1^2 \exp\left\{-i\pi\lambda\Delta\left[\left(\frac{\alpha}{\lambda}\right)^2 + \left(\frac{\beta + \theta}{\lambda}\right)^2\right]\right\} \\
&\quad \times \delta\left(w_x - \frac{\alpha}{\lambda}, w_y - \frac{\beta}{\lambda}\right) \\
&\quad + B_1^2 \exp\left\{-i\pi\lambda\Delta\left[\left(\frac{\alpha}{\lambda}\right)^2 + \left(\frac{\beta - \theta}{\lambda}\right)^2\right]\right\} \\
&\quad \times \delta\left(w_x - \frac{\alpha}{\lambda}, w_y - \frac{\beta - 2\theta}{\lambda}\right) + \cdots \Bigg). \qquad (33)
\end{aligned}
$$

The support of this research through National Science Foundation grant MSS 9109731 and the Research Grant-in-Aid Program (1991) of Auburn University is gratefully acknowledged. The author thanks S. C. Sinha for his helpful suggestions during the analytical research. Some of the experimental results presented here were obtained during the author's postdoctoral research at Caltech, in association with A. J. Rosakis and S. Krishnaswamy.

References

1. H. M. Shang, S. L. Toh, F. S. Chau, V. W. Shim, and C. J. Tay, "Locating and sizing debonds in glassfibre-reinforced plastic plates using shearography," J. Eng. Mater. Technol. **113,** 99–103 (1991).
2. Q. Ru, N. Ohyama, T. Honda, and J. Tsujiuchi, "Constant radial shearing interferometry with circular gratings," Appl. Opt. **28,** 3350–3353 (1989).
3. J. Lewandowski, "Lateral shear interferometer for infrared and visible light," Appl. Opt. **28,** 2372–2379 (1989).
4. D. W. Templeton and Y. Y. Hung, "Shearographic fringe carrier method for data reduction computerization," Opt. Eng. **28,** 30–34 (1989).
5. A. R. Ganeshan, D. K. Sharma, and M. P. Kothiyal, "Universal digital speckle shearing interferometer," Appl. Opt. **27,** 4371–4374 (1988).
6. G. Hausler, J. Jutfless, M. Maul, and H. Weissmann, "Range sensing based on shearing interferometry," Appl. Opt. **27,** 4638–4644 (1988).
7. K. Patorski, "Shearing interferometry and the moiré method for shear strain determination," Appl. Opt. **27,** 3567–3572 (1988).
8. K. Patorski, "Grating shearing interferometer with variable shear and fringe orientation," Appl. Opt. **25,** 4192–4198 (1986).
9. J. Takezaki and Y. Y. Hung, "Direct measurement of strains in plates by shearography," J. Appl. Mech. **53,** 125–129 (1986).
10. Y. J. Chao, M. A. Sutton, and C. E. Taylor, "Interferometric methods for measurement of curvature and twist in thin plates," in *Proceedings of the Society of Experimental Stress Analysis,* B. E. Rossi, ed. Society of Experimental Stress Analysis, Bethel, Conn., 1982), p. 38.
11. K. Patorski, S. Yokozeki, and T. Suzuki, "Collimation test by double grating shearing interferometer," Appl. Opt. **15,** 1234–1240 (1976).
12. D. E. Silva, "Talbot interferometer for radial and lateral derivatives," Appl. Opt. **11,** 2613–2524 (1972).
13. M. V. R. K. Murthy, "The use of a single plane parallel plate as a lateral shearing interferometer with a visible laser source," Appl. Opt. **3,** 531–534 (1964).
14. H. V. Tippur, S. Krishnaswamy, and A. J. Rosakis, "A coherent gradient sensor for crack tip deformation measurements: analysis and experimental measurements," Int. J. Frac. **48,** 193–204 (1991).
15. H. V. Tippur, S. Krishnaswamy, and A. J. Rosakis, "Optical mapping of crack tip deformations using the methods of transmission and reflection coherent gradient sensing: a study of crack tip K_I dominance," Int. J. Fract. **52,** 91–117 (1991).
16. S. Krishnaswamy, H. V. Tippur and A. J. Rosakis, "Measurement of transient crack tip deformation fields using the method of coherent gradient sensing," J. Mech. Phys. Solids **40,** 339–372 (1992).
17. H. V. Tippur and A. J. Rosakis, "Quasi-static and dynamic crack growth along bimaterial interfaces: a note on crack tip field measurements," Rep. SM90-18 (California Institute of Technology, Pasadena, Calif., 1991); Exp. Mech. **31,** 243–251 (1991).
18. K. Iizuka, *Engineering Optics,* 2nd ed. (Springer-Verlag, New York, 1985), Chap. 3, p. 65.

19. J. W. Goodman, *Introduction to Fourier Optics* (McGraw-Hill, New York, 1988), Chap. 5, p. 77.
20. J. D. Gaskill, *Linear Systems, Fourier Transforms and Optics* (Wiley, New York, 1978), Chap. 3, p. 40.
21. M. L. Williams, "On the stress distribution at the base of a stationary crack," J. Appl. Mech. **24,** 109–114 (1959).
22. D. P. Rooke and D. J. Cartwright, *Compendium of Stress Intensity Factors* (Her Majesty's Stationary Office, London, 1975).
23. A. J. Rosakis and K. Ravi Chandar, "On the crack tip stress state: an experimental evaluation of three dimensional effects," Int. J. Solids Struct. **22,** 121–134 (1986).